Monthly Notices
of the
ROYAL ASTRONOMICAL SOCIETY

MNRAS **492,** 480–487 (2020)
Advance Access publication 2019 December 16

doi:10.1093/mnras/stz3497

Uncooled microbolometer arrays for ground-based astronomy

M. F. Rashman,* I. A. Steele, S. D. Bates, D. Copley and S. N. Longmore

Astrophysics Research Institute, Liverpool John Moores University, L3 5RF Liverpool, UK

Accepted 2019 December 10. Received 2019 December 10; in original form 2019 October 14

ABSTRACT

We describe the design and commissioning of a simple prototype, low-cost 10 μm imaging instrument. The system is built using commercially available components including an uncooled microbolometer array as a detector. The incorporation of adjustable germanium reimaging optics rescale the image to the appropriate plate scale for the 2 m diameter Liverpool Telescope. From observations of bright Solar system and stellar sources, we demonstrate a plate scale of 0.75 arcsec per pixel and confirm the optical design allows diffraction limited imaging. We record a ∼10 per cent photometric stability due to sky variability. We measure a 3σ sensitivity of 7×10^3 Jy for a single, ∼0.11 s exposure. This corresponds to a sensitivity limit of 3×10^2 Jy for a 60 s total integration. We present an example science case from observations of the 2019 January total lunar eclipse and show that the system can detect and measure the anomalous cooling rate associated with the features Bellot and Langrenus during eclipse.

Key words: instrumentation: detectors – Moon – infrared: general – infrared: planetary systems.

1 INTRODUCTION

In this paper, we describe the design and commissioning of a simple prototype low-cost mid-infrared (mid-IR) instrument, built using commercially available components and an uncooled microbolometer array as a detector.

Ground-based mid-IR (∼5–20 μm) astronomical observing is very challenging and has been traditionally viewed as impossible for simple, low cost instruments due to the very high thermal background and the requirement for specialist detector systems. Quantitative mid-IR astronomy began in the 1960s (e.g. Low 1961) using heavily cooled single element bolometric detectors on small telescopes. Since the 2000s high-sensitivity, multipixel detectors are in operation at 8-m class facilities such as Gemini (Michelle; Glasse, Atad-Ettedgui & Harris 1997, T-Recs; Telesco et al. 1998), VLT (VISIR; Lagage et al. 2000, MIDI; Leinert et al. 2003), and GTC (CanariCam; Packham et al. 2005). Such instruments are highly complex and the technologies are not easily adapted to smaller 1–2 m class telescopes due to their extensive cooling systems and high detector cost.

Since the 1980s, many advances have been made in the development of mid-IR uncooled microbolometer arrays for defence, security, and industrial applications. These detectors use vanadium oxide (VOx) microbolometers as the focal plane arrays (FPAs) that can deliver noise-equivalent temperature differential (NEdT) measurements of <200 mK (Benirschke & Howard 2017) under factory conditions, and are available integrated into commercial camera systems for <10 000 GBP by manufacturers such as FLIR. In laboratory testing, we have applied analogous, standard astronomical instrumentation techniques to characterize the random and spatial noise present in uncooled microbolometer systems. We have shown that the noise properties of these FPAs are dominated by fixed pattern noise (FPN) that varies on time-scales of <0.5 s (Rashman et al. 2018). This can limit operational NEdT to >50 mK and has the potential to restrict the use of these systems in astronomy. Apart from observations of the moon with very small (<200 mm) telescopes (e.g. Vollmer & Möllmann 2012; Shaw, Nugent & Vollmer 2015), they have never been tested in ground-based applications, although they have been used in some high-altitude experiments (Tsang et al. 2015), where thermal background noise is naturally much lower.

More readily available mid-IR observing resources could have significant scientific impact in time domain astrophysics, where carrying out any kind of monitoring programme of variable sources at such wavelengths is currently impossible. Examples of objects where mid-IR observing is of particular value includes Blazars (where emission of the jet and torus can be traced at 10 μm), dust-forming novae (DQ Her objects), and infrared variables (e.g. VISTA VVV sources). However, uncooled systems such as the one described in this paper are limited to observations of very bright (several hundred Jy) objects and are best suited to monitoring of Solar system objects (comets, asteroids) and galactic objects. While this technology will never be competitive with the cooled technologies employed at the major, large facilities, successful use on 1–2 m class telescopes would provide the opportunity to

* E-mail: m.f.rashman@2016.ljmu.ac.uk

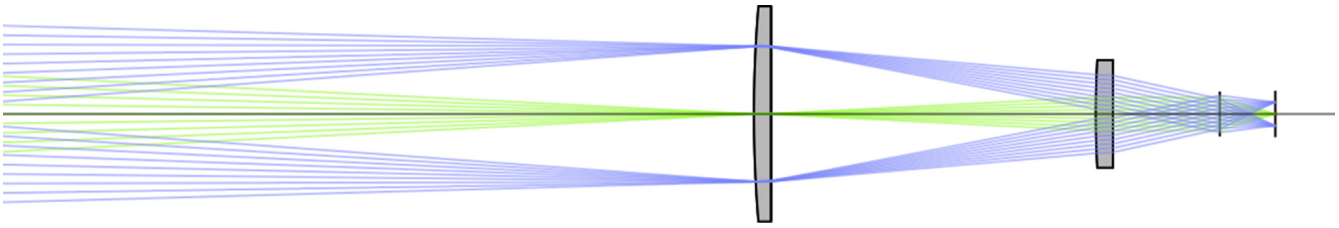

Figure 1. Side view ray trace for on- and off-axis beams of 2.7 arcmin. The 50 mm diameter field and 25 mm diameter collimator lens bend the rays incident off the secondary mirror on to the camera system.

Table 1. Combined optical prescription of the LT and prototype. All dimensions are in mm.

Comment	Type	Radius of curvature	Thickness	Glass	Semidiameter
Source	Standard	inf	inf		0.000
Primary	Asphere	− 12000.0000	0.0000	MIRROR	1000.0000
	Standard	inf	− 4315.385		1000.0000
Secondary	Asphere	− 4813.0000	0.0000	MIRROR	308.0000
	Standard	inf	5615.889		308.0000
Field lens 50 mm	Standard	300.3900	4.000	GERMANIUM	25.000
	Standard	inf	76.000		25.000
Collimator 25 mm	Standard	225.0000	4.000	GERMANIUM	12.500
	Standard	inf	25.000		12.500
Lens	Paraxial	inf	13.000		5.200
Detector	Standard	inf	0.000		5.400

expand at low cost the availability of mid-IR observing of these bright objects. In addition, greater availability of mid-IR observing facilities on smaller telescopes could provide a key resource to train students and early career researchers on mid-IR observing techniques and data analysis.

In this paper, we present our prototype: a small, uncooled, *N*-band (∼10 μm) instrument, constructed from 'off the shelf' components. We provide the results of a week long programme of observations conducted to test the system sensitivity and stability, and determine the feasibility of using this technology in 'facility' class instruments for small telescopes. As an example science case we present observations of the cooling of lunar surface features during the 2019 January lunar eclipse.

2 OPTICAL DESIGN

The prototype was initially designed for use on the Liverpool Telescope (LT; Steele et al. 2004). However, the nature of the adjustable reimaging optics allows this design to be adapted for other 1–2 m class telescopes with a similar focal ratio. The LT is an f/10 telescope with a Ritchey–Chrétien design. It is comprised of a 2 m concave primary mirror, a 0.65 m convex secondary mirror and a 0.2 m science fold mirror at a 45° angle at the Cassegrain focus to direct light on to detectors. The LT has a 10 μm diffraction limit of 1.23 arcsec.

The prototype *N*-band instrument was built around a commercial mid-IR imager, produced by the manufacturer FLIR. This pre-assembled system is comprised of their Tau 2 core; a vanadium oxide microbolometer (640 × 512 pixels of dimensions 17 × 17 μm), and a 13 mm focal length lens of unspecified prescription. To rescale the image to an appropriate plate scale for use on a telescope, the 13 mm focal length lens and detector were modelled as a paraxial system and ray tracing analysis for on- and off-axis light was conducted. This optical design can be seen in Fig. 1. The optical prescription of the LT and prototype can be seen in Table 1.

This prescription was then translated into a low-cost, 'off the shelf' system comprised of an Edmund Optics 50 mm diameter, 100 mm focal length, 8–12 μm, AR coated, germanium plano-convex field lens and a Thorlabs 25 mm diameter, 75 mm focal length, 7–12 μm, AR coated, germanium plano-convex collimator lens. Both lenses act to collimate the light collected with the LT on to the FLIR imaging system. Both lenses have an antireflection coating that reduces reflection losses to <3 per cent in the 8–12 μm wavelength range. When mounted to the LT, the prototype has a plate scale of 0.75 arcsec per pixel, with two pixels sampling the 10 μm diffraction limit of the LT. In practice, we found that, as there was uncertainty in the location of the pupil and the presence of an aperture stop within the FLIR system, the imaging field of view (FOV) reduced to a circular aperture of 500 pixel diameter. This results in a ∼6.25 arcmin diameter FOV at LT.

Computed spot diagrams for on-axis and ±2.7 arcmin off-axis rays are shown in Fig. 2. These figures highlight the off-axis aberration that is inherent in the optical design. The prototype has an 80 per cent geometric encircled energy (GEE) diameter of <1.1 arcsec for on-axis rays and <3.1 arcsec for off-axis rays, as seen in Fig. 3. Assuming a 2D Gaussian profile, this corresponds to a spatial full width at half-maximum (FWHM) of <0.7 and <2.0 arcsec for on- and off-axis rays, respectively. Two pixels was therefore predicted to sample the diffraction limit for on-axis rays, with slightly worse performance off-axis.

3 MECHANICAL DESIGN

The overall aim of this project was to build a low-cost mid-IR detector that could be constructed from commercially available components. As a result of this, we opted to translate the optical design into a lens system using tubing purchased from Thorlabs. The field lens and collimator were housed in an anodized aluminium tube of length 114 mm and diameter 50 mm. The field lens was secured at the front of the lens system. The collimator was secured

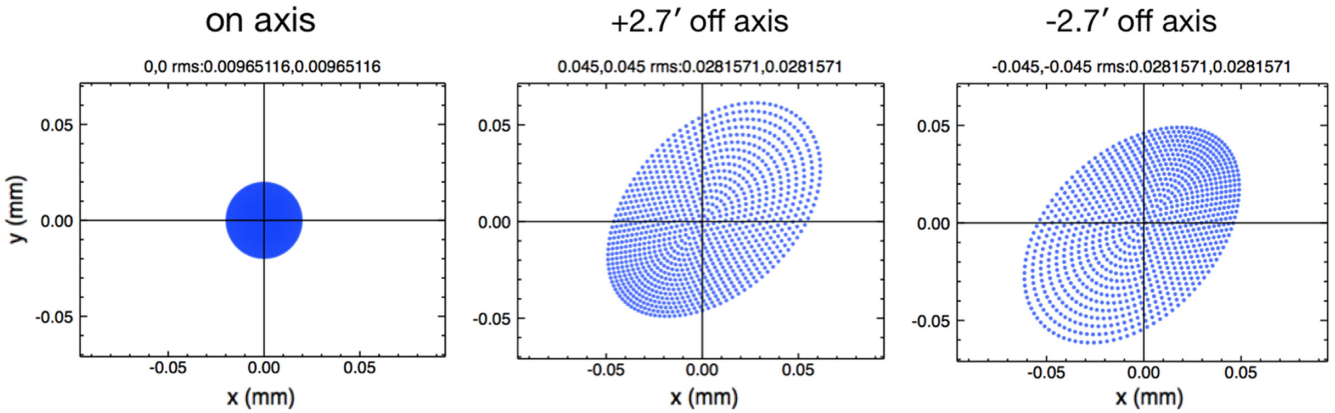

Figure 2. Spot diagrams generated assuming a 10 μm wavelength point source, with no atmospheric seeing, on-axis and ±2.7 arcmin off-axis. *x*- and *y*-axes are mm in the focal plane, where 0.11 mm ∼4.4 arcsec.

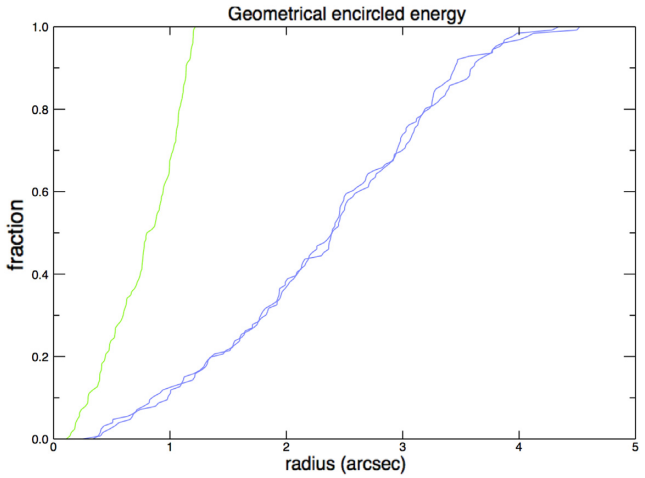

Figure 3. The geometrical encircled energy for, from left to right, on-axis and ±2 arcmin off-axis rays for a wavelength of 10 μm.

76 mm behind the field lens inside the tubing, using a 25–50 mm adjustable adaptor to allow small changes to the focus of the lens. Two custom pieces milled from low-grade aluminium were commissioned. These pieces acted to secure placement of the FLIR 13 mm lens, ∼25 mm from the collimator and to attach the entire prototype ∼75 mm from the telescope mounting flange, roughly at the telescope focal point. When constructed, the prototype has dimensions of ∼171 mm × 60 mm and a weight of 0.33 ± 0.05 kg. This makes the prototype a very compact system and suitable for mounting on 1–2 m class telescopes with a sufficient counter-balance.

The LT is a fully robotic system and therefore remote access to the instrument was essential. The ThermalCapture Grabber USB OEM was installed on the back of the FLIR system, which, paired with a Beelink J45 Mini PC running Xubuntu, allowed for remote control of data acquisition. Software was designed to collect data by downloading the image at a frequency of 9 Hz, whilst simultaneously displaying a live feed of observations with a delay of <1 s. This was beneficial when deploying the prototype to be able to determine parameters such as the optimum focus of the secondary mirror and telescope pointing during operation. A live feed also allowed for manual nodding of the telescope that was important for centring calibration sources and mapping non-sidereal, non-point sources (i.e. the moon).

4 CALIBRATION

The FLIR system self-calibrates by introducing an opaque shutter between the 13 mm lens and the detector. This flat-field calibration acts to correct any non-uniform changes in response across the detector FPA during operation. The shutter deploys at a pre-defined period of ∼2.5 min, but can also be triggered by any significant changes in environment or detector temperature. By applying this correction, the offset correction factors of the microbolometer elements are reset to factory standard to reduce thermal drift, which causes counts to increase steadily until the camera self-calibrates.

Read out values $(x, y)_T$ are pre-scaled by the system to have a linear relationship with temperature T in Kelvins, where

$$T = (x, y)_T \times 0.04. \quad (1)$$

To approximate these values, as un-scaled counts we have assumed the following relation:

$$\text{counts} = (x, y)_T^4. \quad (2)$$

Once approximated as counts, a scaling factor of 1.85 is introduced to correct for the f/ratio difference between the raw imaging system using the supplied camera lens and that via the optical system.

Mid-IR background can be several orders of magnitude brighter than most astronomical sources (Pietrow, Burtscher & Brandl 2019) and arises primarily from thermal emission from the sky, telescope, and any structures visible to the detector (e.g. the optics and electronics). Temperature fluctuations in these components gives rise to noise and considerable background variability. Sky emission (and transmission) has by far the highest spatial and temporal variability, with variations occurring on subsecond time-scales. Telescopic emissions are slightly more stable, with variations occurring on time-scales of tens of seconds to minutes (Mason et al. 2008). IR optimized telescopes deploy chopping/nodding mechanisms frequently during observations to characterize and remove atmospheric and telescopic contributions. For the purpose of testing the prototype, and due to the LT not being optimized for IR observations, we were unable to deploy a chopping/nodding regime to remove sky contributions. Sky flats were taken prior to, and subtracted off, observations of point sources. However, for extended sources (i.e. the moon), background reduction occurred post-observation, during the data reduction stage.

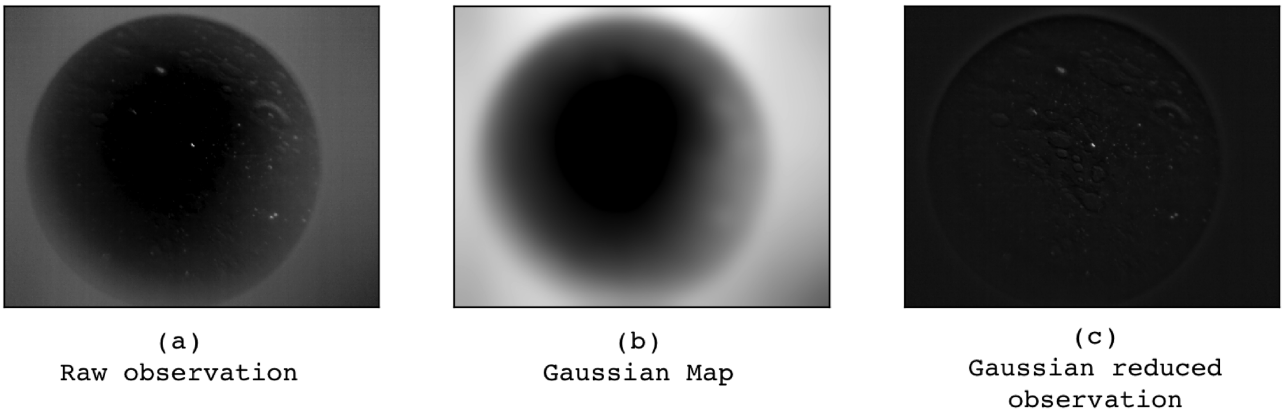

Figure 4. Observations were reduced using Gaussian Maps to remove the significant FPN present in the system. Panel (a) is a raw observation of the eclipsing moon, panel (b) is the Gaussian map produced from this exposure with $\sigma = (15, 15)$ pixels, and panel (c) is the resultant exposure reduced by applying equation (3).

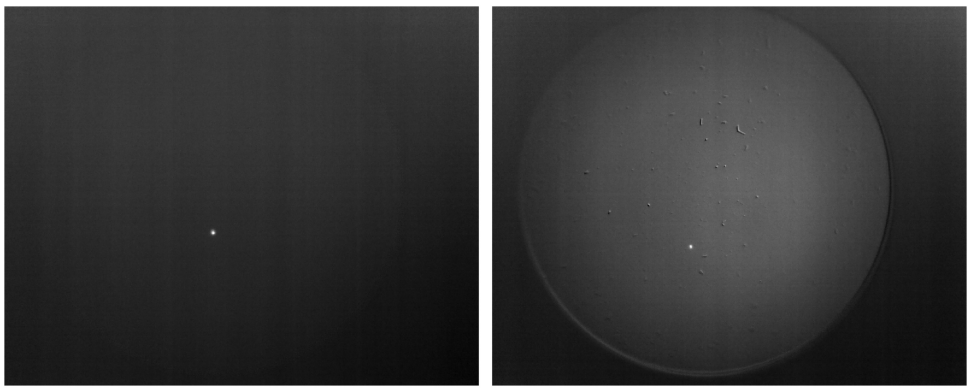

Figure 5. Observations of (a) Mars and (b) IRC+10216 taken on 2019 January 22. Both (a) and (b) are median stacks created from 1000 non-Gaussian corrected, flat subtracted observations.

Observations taken with uncooled microbolometer systems are generally dominated by FPN. FPN is spatial noise that is generally static over short time-scales, and arises from detector imperfections and variations in the responsivity, gain, and noise of FPA elements (Rashman et al. 2018). FPN results in a spatially heterogeneous response across the FOV. Getting a measure of the FPN present at any given time is difficult as FLIR systems have a limited range of viewable scene temperature and therefore are unable to be calibrated using exposures of supercooled surfaces. Without the means to correct for FPN, Gaussian maps were used to 'flat-field' observations to correct for the large-scale variations across the detector (e.g. arising from vignetting or spatially heterogeneous variation in sensitivity) but not for the effects of FPN. For each exposure $S_{x,y}$, a Gaussian map was created by applying a multidimensional, Gaussian filter with $\sigma = (15, 15)$ pixels. The resulting Gaussian map $g_{x,y}$ was used to reduce the exposure, prior to data analysis, as follows:

$$I_{x,y} = \frac{S_{x,y}}{g_{x,y}} \cdot \bar{S}_{i,j} \tag{3}$$

where $I_{x,y}$ is the corrected exposure and $\bar{S}_{i,j}$ is the mean value inside the imaging aperture. The mean of the entire frame $\bar{S}_{x,y}$ is not used to re-scale values as the outer aperture contains no sky signal and is likely to skew values towards telescopic background. Fig. 4 illustrates this process: panel (a) is a raw observation of the eclipsing moon. There is considerable FPN structure present in the FOV that can be seen as large light and dark regions. This type of FPN is characteristic of that found in all our un-reduced data. Panel (b) is the unique Gaussian map created from panel (a). Panel (c) is exposure (a) after it has been fully reduced by applying equation (3).

5 COMMISSIONING AND ON SKY TESTING

The prototype was installed on the LT on 2019 January 19. It was deployed over three nights, including during the Lunar eclipse.

5.1 Photometric accuracy and stability

To determine the photometric performance of the system, observations were taken of two bright mid-IR sources: Mars and IRC+10216 (Neugebauer & Leighton 1969; see Fig. 5). Offsetting the telescope pointing during our observations of Mars confirmed a pixel scale of 0.75 arcsec per pixel for the system. IRC+10216 was observed at an FWHM of ∼2 pixels confirming the optical design allows diffracted limited imaging. Fig. 6 shows the variation in FWHM and counts of IRC+10216 over a short period of 348 s, taken shortly after a flat-field correction to reduce the effect of thermal drift. The ∼10 per cent variability in these observations can

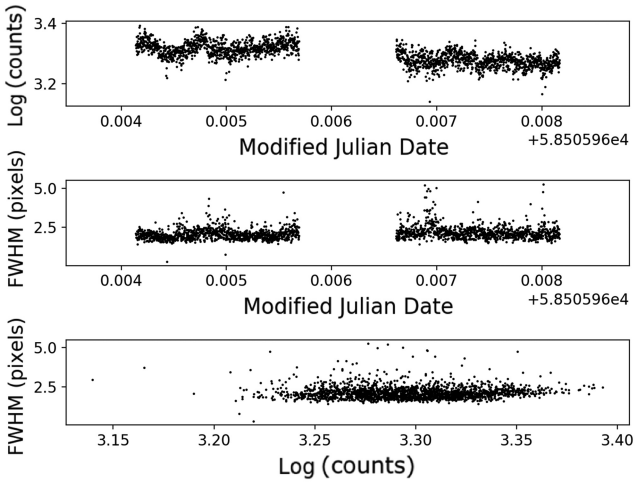

Figure 6. The variation in background-subtracted counts and FWHM for observations of IRC+10216 taken on 2019 January 22. Observations appear reasonably stable, with ∼10 per cent variability (determined from the rms of the sample) attributed to the highly variable seeing conditions on this date, although there is no formal correlation between FWHM and counts (with a Spearman rank coefficient value of −0.03).

be attributed to the sky variations during observing and represent a basic estimate of the system stability.

The system accuracy was tested by comparing known and observed values of 12 μm flux for Mars and IRC+10216. A 12 μm flux of 4.75×10^4 Jy was obtained for IRC+10216 from the IRAS catalogue of point sources (Beichman et al. 1988). IRC+10216 is a known variable source however for this purpose, we approximated 12 μm flux as constant. The apparent brightness of Mars depends on the sub-Earth longitude of the illuminated disc (Mallama 2007) and therefore varies seasonally and as a function of viewing angle. To determine an approximate value of 12 μm flux on our observing date for Mars, we obtained brightness temperatures at 12 and 450 μm from models derived by Wright (1976), and implemented in the FLUXES routine developed for JCMT (Dempsey et al. 2013). These brightness temperatures were then used to calculate a 12 μm flux of 76147.5 Jy using the following equation:

$$S_\nu = \frac{2h\nu^3}{c^2} \frac{\Omega_p}{\exp\left(\frac{h\nu}{kT_\nu}\right) - 1} \tag{4}$$

where ν is the given frequency in GHz; S_ν is the integrated flux density of Mars; Ω_p is the solid angle subtended by Mars from Earth; T_ν is the brightness temperature; and h, k, and c are the Planck constant, Boltzmann constant, and speed of light, respectively. The flux ratio of IRC+10216/Mars for catalogue and observed values were calculated as 0.62 and 0.72, respectively. These values are consistent with a 15 per cent uncertainty on photometric accuracy with the caveat that both sources are known to be variable.

5.2 Sensitivity

Our observations of IRC+10216 were used to determine the sensitivity of the system. Measurements of the object were obtained using apertures with a 1.5 pixel radius and sky background counts were estimated for subtraction using an annulus of 1.5–2 pixel radius. These apertures were selected using a curve of growth technique to maximize SNR. Over a short duration (∼10 s) of exposures, which appear to be unaffected by sky variation, IRC+10216 has SNR = 21. Assuming our observations are sky noise dominated, then SNR will be proportional to source flux. For a single exposure (with exposure time $t \sim 1/9$ s), a 3σ detection would correspond to a background-subtracted flux seven times fainter than those observed in Fig. 6, i.e. $\sim 7 \times 10^3$ Jy. In theory, the sensitivity can be improved by stacking exposures, with a 60 s exposure stack having a predicted 3σ detection for a source 163 times fainter than IRC+10216, i.e. $\sim 3 \times 10^2$ Jy. In practice, without a nodding/chopping system, this limit is unlikely to be reached with the current set-up

5.3 Lunar eclipse observation

Observations of the 2019 January 21 eclipse and full moon (±2 d) were taken to obtain measurements of surface temperature and its variability during an eclipse. The eclipsing lunar disc has been well studied since the first observations of thermal anomalies in 1960 (Shorthill, Borough & Conley 1960; Saari & Shorthill 1963; Shorthill & Saari 1965; Fudali 1966; Saari, Shorthill & Deaton 1966; Hunt, Salisbury & Vincent 1968; Shorthill & Saari 1972; Winter 1972; Fountain et al. 1976; Lawson et al. 2003; Price, Mizuno & Murdock 2003).

The general thermophysical properties of the lunar surface have been well mapped in the mid-IR (see Paige et al. 2010; Vasavada et al. 2012; and references therein). The low thermal conductivity of the fine-grained, regolith that makes up the upper ∼0.02 m surface layer, results in extreme diurnal temperature variation. During lunar daytime, illuminated surfaces are close to radiative equilibrium and high surface temperatures (approaching 400 K) are a result of incident solar flux. Comparatively, during a lunar eclipse or during lunar night-time, with no incident solar radiation and no atmosphere to trap heat, surface temperatures drop by ∼300 K. The moon also shows significant topographic heterogenity. This results in high spatial variation in the thermophysical properties of lunar surface features.

A simple temperature model for the lunar surface (equation 5), derived by Shaw et al. (2015), can be used to estimate the expected temperature of the lunar surface, T_m at any given time; where E_m is the spectrally averaged solar irradiance at the surface (adjusted for seasonal variations in earth sun distance). The subsolar point, where lunar latitude angle $\varphi = 0$, can be used to approximate the maximum temperature of the lunar surface, $T_{\max}$. Latitudinal and diurnal variation in T_m across increasing lunar radius is mostly controlled by angular distance to the subsolar point:

$$T_m(\varphi) = \left(\frac{E_m \cos(\varphi)}{\sigma}\right)^{1/4} = T_{\max} \cos^{1/4}(\varphi). \tag{5}$$

Using equation (5), we can calculate that the expected maximum temperature of the lunar surface on the 2019 January 19 and 22, two days either side of the full moon, is 396.8 K. The radiation incident on the LT can be modelled as

$$I(\phi_z, \lambda) = I_0 \, \mathrm{e}^{-AM(\phi_z)\cdot\tau_N(\lambda)}, \tag{6}$$

where $AM(\phi_z)$ is the airmass for a given zenith angle and $\tau_N(\lambda)$ is the normal optical thickness. $\tau_N(\lambda)$ is dependent on the atmospheric transmission for a given wavelength. For mid-IR wavelengths, the theoretical atmospheric transmission at normal incidence ranges from 0.70 to 0.75 (Vollmer & Möllmann 2012). Equation (6) therefore gives an expected value of observed lunar surface temperature of 362.9 K. Our observations on these dates recorded an average temperature of 350 ± 6 K. This slightly lower value is likely due to losses in the telescope and instrument optics.

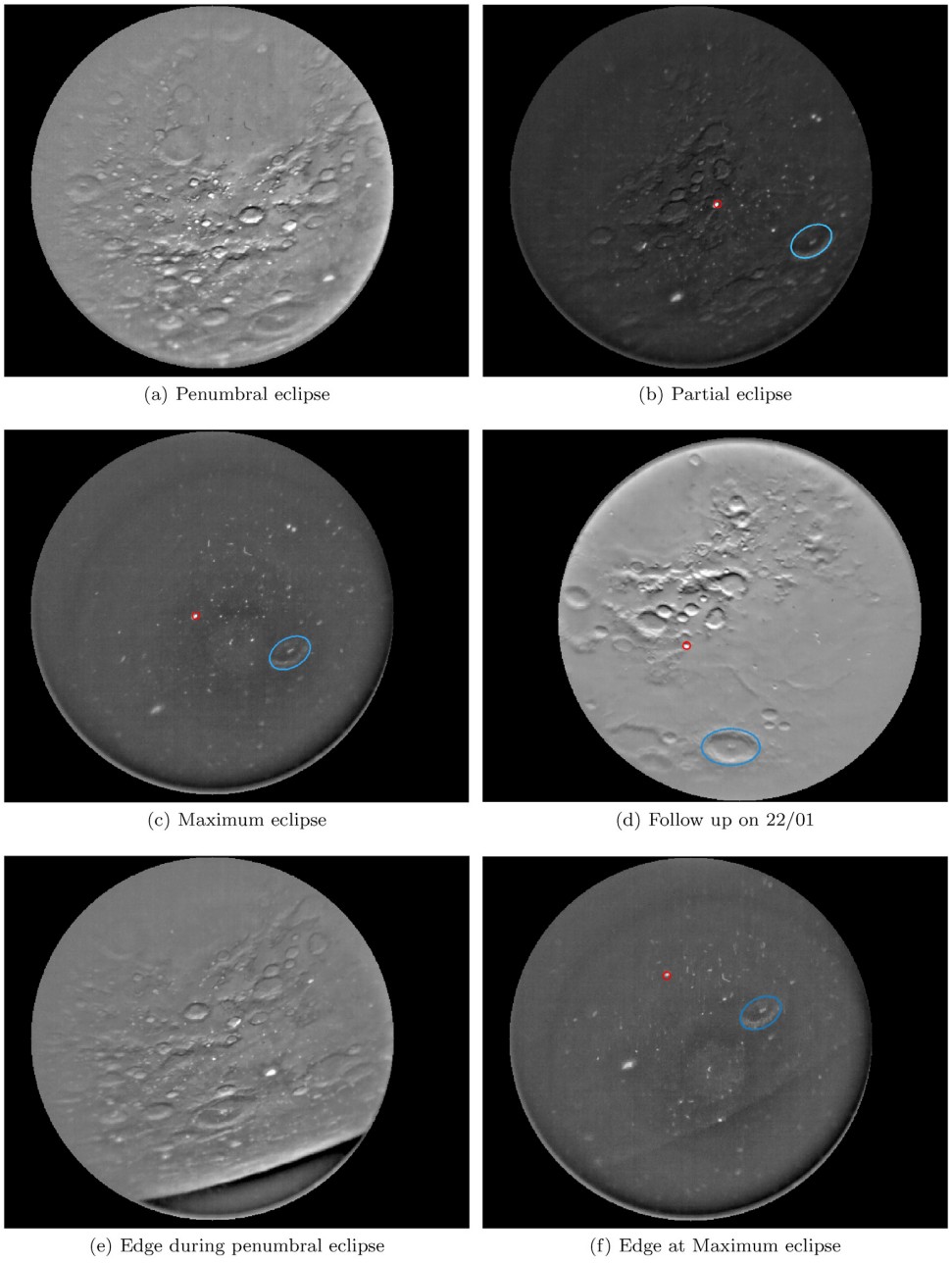

(a) Penumbral eclipse (b) Partial eclipse

(c) Maximum eclipse (d) Follow up on 22/01

(e) Edge during penumbral eclipse (f) Edge at Maximum eclipse

Figure 7. Observations of the moon during the lunar eclipse and follow-up on 2019 January 22. Lunar limb observations highlight the change in temperature between early and maximum eclipse. Where possible, the locations of two craters, Bellot (red) and Langrenus (blue), have been indicated. The presence of dust on the field lens can masquerade as bright features on the lunar surface, this can be seen very clearly in image (f) where bright features lie beyond the limb. As these dust contaminants remain fixed in position in the FOV, genuine bright features have been confirmed through their movement with the lunar surface. For scale, one pixel ∼4 km on the lunar surface.

Observations of partial, full and maximum phases of the lunar eclipse were taken (see Fig. 7). Significant heat loss occurs prior to this, during the penumbral phase (Vollmer & Möllmann 2012). Unfortunately, we were unable to obtain enough sequential observations of the same region due to poor weather conditions to include these exposures in our analysis.

Visually, the change in lunar surface from partial eclipse onwards is quite significant. As the eclipse reaches totality, the different thermophysical properties of features of the lunar surface become very apparent. During this time, many features become unobservable. However, the hundreds of thermal anomalies that were first seen by Shorthill et al. (1960) appear as very bright 'hot spots' during partial eclipse and remained bright throughout totality. During our observations, we focused on several lunar features in the mare Fecunditatis region (7.8°S, 51.3°E). Analysis was conducted for two craters; Bellot (12.49°S, 48.2°E) and Langrenus (9°S, 62°E). Langrenus is an early Copernican crater with a faint ray pattern, a high albedo, a central peak of brecciated bedrock and a moderate thermal anomaly (Shorthill & Saari 1972). Bellot is a smooth, dark haloed crater with a high albedo, likely a result of freshly exposed, brecciated rock (Elston & Holt 1967), resulting in a significant thermal anomaly.

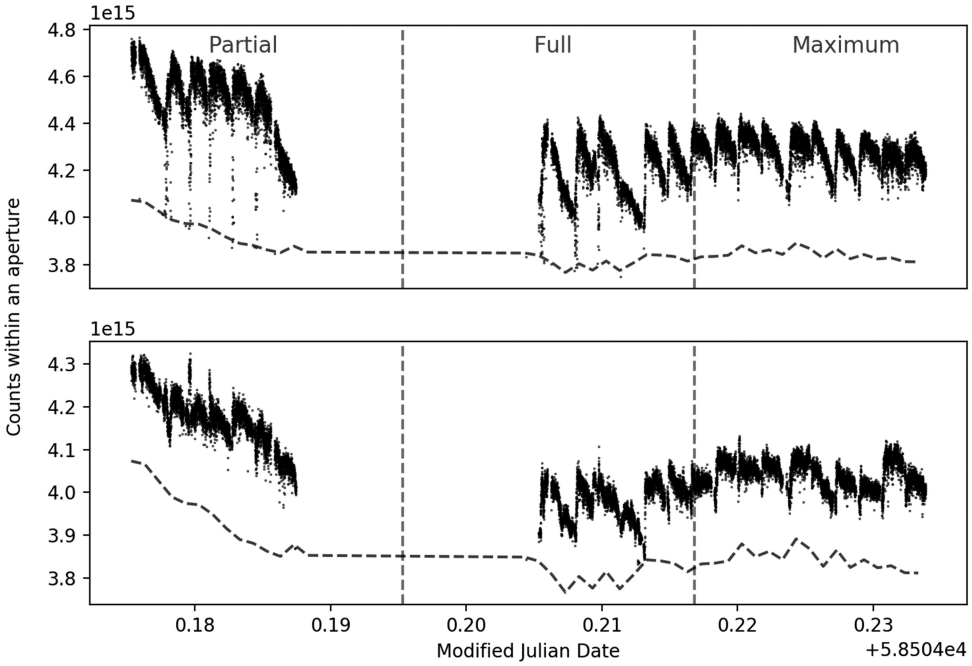

Figure 8. Observations of Bellot (top) and Langrenus (bottom) during the lunar eclipse on 2019 January 21. Count values are maximum values within an aperture. Both curves are plotted with background counts (dashed line). A large period between partial and full eclipse went unobserved due to a sudden spike in humidity that halted observation. The periodic fluctuating pattern present in all curves is thermal drift. This is described in more detail in Section 4.

To conduct data analysis for ∼30 000 eclipse exposures, we employed a semi-automated feature tracking regime to determine the approximate centre of the brightest source, Bellot. The coordinates of Bellot were then used to anchor the movement of other features in the FOV. Each exposure was reduced, and raw values converted to counts, as described in Section 4. Counts for each feature were obtained by taking the maximum value from apertures containing each feature. A circular aperture with 5 pixel diameter was used for Bellot and an elliptical aperture with 30 pixel semimajor axis, and $\pi/3$ rotation for Langrenus.

Analysis of observations during partial eclipse showed approximate temperature loss rates of 0.98 K per minute for Bellot and 0.50 K per minute for Langrenus. Comparatively, the average heat loss in regions with no 'hot spots' or crater features occurred at a rate of 0.26 K per minute. Fig. 8 are count measurements of Bellot (top) and Langrenus (bottom) during the eclipse. The dashed line in both plots represents the background counts recorded from an aperture with 10 pixel diameter, in a region of mare with no crater features. The apparent plateau in all three curves is likely a result of telescope and system emissions limiting the range of temperatures that can be recorded.

The low conductivity of the upper lunar regolith results in little exchange of energy between warmer subsurface and surface layers. As a result, the lunar surface cannot maintain surface temperatures without incident radiation from the Sun. Couple this with the high emissivity of the lunar surface around full moon (ϵ ∼0.97; Shaw et al. 2015), we can approximate that the energy required ΔE, to maintain the lunar daytime temperature T, is equal to the energy release over time dt, during eclipse:

$$\Delta E = mc\Delta T\,\mathrm{d}t = \epsilon\sigma T^4, \tag{7}$$

where m is the mass, c is the specific heat capacity, and σ is the Stefan–Boltzmann constant. We can derive the following differential equations from equation (7) for a temperature change of T_1–T_2 in time t_1 to t_2:

$$\int_{T_1}^{T_2} \frac{1}{T^4}\,\mathrm{d}T = \int_{t_1}^{t_2} \frac{\epsilon\sigma}{mc}\,\mathrm{d}t. \tag{8}$$

The bulk density of the lunar regolith sharply increases at a depth of ∼0.02 m. So, solving equation (8) for a 1 m^2 area, we can calculate a naive estimate of specific heat capacity c, for different regions in our observations. For Bellot and Langrenus, we calculate a specific heat capacity of 2.3 and 4.1 kJ kg^{-1} K^{-1}, respectively. There is a discrepancy between our naive estimates and the heat capacity of the lunar regolith quoted in literature. Analysis of the Apollo 14, 15, and 16 samples recorded specific heat capacities of between 0.21 and 0.8 kJ kg^{-1} K^{-1} (Hemingway, Robie & Wilson 1973). More recent studies of sintered Australian Lunar Regolith Simulant (ALRS-1) have found values of up to 1.63 kJ kg^{-1} K^{-1} (Bonanno, Li & Bernold 2014). The diasgreement between these values and our own could be largely in part due to the Apollo samples being collected from regions different than ours. This would be applicable to the values obtained from ALRS-1, as it is created to have a chemical composition comparative to Apollo 12 samples. We also make several assumptions in our calculations that may not be applicable to our crater regions. The quoted emissivity and depth values are approximated across the entire lunar surface, but these are known to vary with region age and regolith material. It is also possible that the shape of both craters contributes to the storage of heat during eclipse.

6 DISCUSSION/CONCLUSION

In this paper, we have presented a prototype instrument that adapts mid-IR uncooled microbolometer technology for use on ground telescopes in the 1–2 m class. For this purpose, additional optics were designed to rescale the image on to the detector to optimally sample the diffraction limit. We opted to design and build

the instrument from commercially available units, at a low cost. The instrument was tested on the LT over 3 d in 2019 January. A small programme of observations of Solar system and stellar objects was conducted. From these observations, we confirmed a plate scale of 0.75 arcsec pixel^{-1} and obtained a measure of the ∼10 per cent photometric stability and performance of the instrument. We recorded a 3σ sensitivity of $\sim 7 \times 10^3$ Jy for a single exposure corresponding to a sensitivity limit of $\sim 3 \times 10^2$ Jy for an integration time of 60 s. Using the IRAS point source catalogue v2.1 (Beichman et al. 1988) we can see that such a limit would make a further ∼163 extra-solar sources observable with the current instrument set-up. Given the IRAS point spread function at 12 μm corresponds to an FWHM of <16 arcsec some of these sources may be extended and therefore our calculation is an estimate of the upper limit of observable sources. For observations of bright asteroids, such as Ceres, this limit would have to be improved by a factor of 2 (Müller & Lagerros 2002). Observations of the eclipsing moon are presented as a science case. In general, the overwhelming sky and telescopic emission limited observations to very bright mid-IR sources and made data reduction difficult. The germanium foreoptics have significant transmission into the wings of the *N* band. As a result, there is likely excess sky noise limiting our observations that could be improved with the inclusion of a narrow bandpass filter. We aim to further develop the prototype to include a chopping/nodding regime to test whether the stability and sensitivity of the system can be improved and increase the number of observable sources.

ACKNOWLEDGEMENTS

MFR and IAS gratefully acknowledge funding from the Royal Astronomical Society Patricia Tomkins Instrumentation award. The LT is operated by Liverpool John Moores University at the Spanish Observatoria del Roque de los Muchachos of the Instituto de Astrofísica de Canarias in La Palma, with financial support from the UK Science and Technology Facilities Council. MFR is funded by a Liverpool John Moores University FET/SCS PhD scholarship. This research has made use of the NASA/ IPAC Infrared Science Archive, which is operated by the Jet Propulsion Laboratory, California Institute of Technology, under contract with the National Aeronautics and Space Administration. This research made use of ASTROPY, a community-developed core PYTHON package for Astronomy (Astropy Collaboration et al. 2013; Price-Whelan et al. 2018).

REFERENCES

Astropy Collaboration et al., 2013, A&A, 558, A33
Beichman C. A., Neugebauer G., Habing H. J., Clegg P. E., Chester T. J., 1988, Infrared Astronomical Satellite (IRAS) Catalogs and Atlases. Vol. 1: Explanatory Supplement, IRSA, California
Benirschke D., Howard S., 2017, Opt. Eng., 56, 1
Bonanno A. C., Li A., Bernold L., 2014, Earth and Space 2014: Engineering for Extreme Environments, Comparative Specific Heat Capacity Analysis for Lunar In-Situ Manufacture of Thermal Energy Storage, ASCE , Virginia, p. 434
Dempsey J. T. et al., 2013, MNRAS, 430, 2534
Elston D. P., Holt H. E., 1967, Abstracts for 1967, Vol. 57, Geological Society of America, Colorado
Fountain W. F., Raine W. L., Fountain J. A., Jones B. P., Watkins J. R., 1976, Moon, 15, 421
Fudali R. F., 1966, Icarus, 5, 536
Glasse A. C., Atad-Ettedgui E. I., Harris J. W., 1997, in Ardeberg A. L., ed., Proc. SPIE Conf. Ser. 2871, Optical Telescopes of Today and Tomorrow. SPIE, Bellingham, p. 1197
Hemingway B. S., Robie R. A., Wilson W. H., 1973, Lunar Planet. Sci. Conf. Proc., 4, 2481
Hunt G. R., Salisbury J. W., Vincent R. K., 1968, Science, 162, 252
Lagage P. O., Durand G. A., Lyraud C., Rio Y., Pel J. W., de Haas J. C., 2000, in Iye M., Moorwood A. F., eds, Proc. SPIE Conf. Ser. 4008, Optical and IR Telescope Instrumentation and Detectors. SPIE, Bellingham, p. 1120
Lawson S. L., Rodger A. P., Henderson B. G., Bender S. C., Lucey P. G., 2003, in Mackwell S., Stansbery E., eds, Lunar and Planetary Science Conference, USRA, Houston, p. 1761
Leinert C. et al., 2003, Ap&SS, 286, 73
Low F. J., 1961, J. Opt. Soc. Am., 51, 1300
Mallama A., 2007, Icarus, 192, 404
Mason R., Wong A., Geballe T., Volk K., Hayward T., Dillman M., Fisher R. S., Radomski J., 2008, in Brissenden R. J., Silva D. R., eds, Proc. SPIE Conf. Ser. 7016, Observatory Operations: Strategies, Processes, and Systems II. SPIE, Bellingham, p. 616
Müller T. G., Lagerros J. S. V., 2002, A&A, 381, 324
Neugebauer G., Leighton R. B., 1969, NASA SP, 3047
Packham C., Telesco C. M., Hough J. H., Ftaclas C., 2005, Rev. Mex. Astron. Astrofis., 24, 7
Paige D. A. et al., 2010, Space Sci. Rev., 150, 125
Pietrow A. G. M., Burtscher L., Brandl B., 2019, Res. Notes Am. Astron. Soc., 3, 42
Price S. D., Mizuno D., Murdock T. L., 2003, Adv. Space Res., 31, 2299
Price-Whelan A. M. et al., 2018, AJ, 156, 123
Rashman M. F., Steele I. A., Burke C., Longmore S. N., Wich S., 2018, in Holland A. D., Beletic J., eds, Proc. SPIE Conf. Ser. 10709, High Energy, Optical, and Infrared Detectors for Astronomy VIII. SPIE, Bellingham, p. 667
Saari J. M., Shorthill R. W., 1963, Icarus, 2, 115
Saari J. M., Shorthill R. W., Deaton T. K., 1966, 5, 635
Shaw J., Nugent P., Vollmer M., 2015, Appl. Opt., 54, B64
Shorthill R. W., Saari J. M., 1965, Science, 150, 210
Shorthill R. W., Saari J. M., 1972, in Kopal Z., ed., Advances in Astronomy and Astrophysics, Vol. 9, Elsevier, Netherlands, p. 149
Shorthill R. W., Borough H. C., Conley J. M., 1960, PASP, 72, 481
Steele I. A. et al., 2004, in Oschmann J. M., Jr, ed., Proc. SPIE Conf. Ser. 5489, Ground-based Telescopes. SPIE, Bellingham, p. 679
Telesco C. M., Pina R. K., Hanna K. T., Julian J. A., Hon D. B., Kisko T. M., 1998, in Fowler A. M., ed., Proc. SPIE Conf. Ser. 3354, Infrared Astronomical Instrumentation. SPIE, Bellingham, p. 534
Tsang C. C. C., Durda1 D. D., Ennico K. A., Less J., Propp T., Olkin C. B., Stern S. A., 2015, 46th Lunar and Planetary Science Conference, USRA, Maryland
Vasavada A. R., Bandfield J. L., Greenhagen B. T., Hayne P. O., Siegler M. A., Williams J.-P., Paige D. A., 2012, J. Geophys. Res.: Planets, American Geophysical Union, Washington DC, p. E00H18
Vollmer M., Möllmann K. P., 2012, Eur. J. Phys., 33, 1703
Winter D. F., 1972, in Kopal Z., ed., Advances in Astronomy and Astrophysics, Vol. 9, Elsevier, Netherlands, p. 203
Wright E. L., 1976, ApJ, 210, 250

This paper has been typeset from a TEX/LATEX file prepared by the author.